Amorphous TiO_2 Inverse Opal Anode for High-rate Sodium Ion Batteries

*Min Zhou[a,1], Yang Xu[a,1], Chengliang Wang[a], Qianwen Li[a], Junxiang Xiang[b], Liying Liang[a], Minghong Wu[c], Huaping Zhao[a], Yong Lei[a]**

[a]Institute of Physics and Macro- and Nanotechnologies MacroNano® (IMN & ZIK), Ilmenau University of Technology, 98693 Ilmenau, Germany.

[b]Department of Materials Science and Engineering, University of Science and Technology of China, Hefei, 230026, P. R. China

[c]Institute of Nanochemistry and Nanobiology, School of Environmental and Chemical Engineering, Shanghai University, 200444 P. R. China

*Corresponding author. E-mail address: yong.lei@tu-ilmenau.de.

[1]Dr. M. Zhou and Dr. Y. Xu contributed equally to this work.

Keywords: sodium ion battery, amorphous, TiO_2, inverse opal, energy storage

Abstract

Potential applications of sodium-ion batteries (SIBs) have motivated significant research interest in grid-scale energy storage. However, large radius of Na ions results in different electrochemical behaves. Therefore, synergistic understanding of the differences is greatly interested for future development of SIBs. Surface availability for ions with poor affinity to electrode materials is critical to rate performance in SIBs, but yet has rarely been reported. Here, to overcome the obstacles of material platform, amorphous TiO_2 inverse opal is employed as a proof-of-concept prototype to illuminate the effects of surface ion availability and its relationship between solvent wettability and rate capability. Within expectation, superior rate capabilities are

achieved in return for enhanced solvent wettability, regardless of the type of electrolyte and the ion concentration in electrolyte. Even when the anode is cycled at a current density as high as 5000 mA g^{-1}, the reversible capacity could still retain a high value of ~113 mA h g^{-1}. Our concept opens up a promising avenue to realize full potential of designing electrode materials for SIBs by adjusting the surface kinetics. This understanding shall extend the design principle to electrode materials for highly effective energy storage using other transport ions and other storage mechanisms.

Graphical Abstract

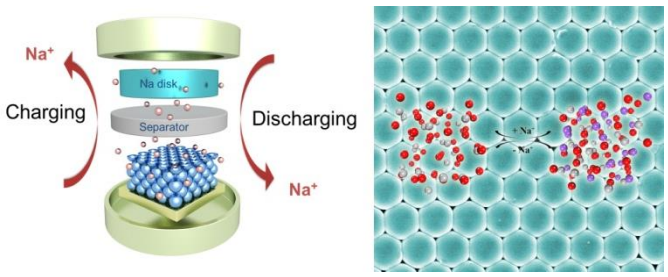

1. Introduction

Demands of electronic energy storage keep increasing due to the requirements for electronic devices, vehicles and renewable energy commercialization.[1-4] Li ion battery (LIB) as a prevailing technology therefore has powered most modern-day electronic devices.[5-7] Despite substantial research, issues like the accessible global lithium, safety and cost still remain to be fully solved. Hence, the quest for alternative energy source motivates significant momentum. Abundant and environmentally benign sodium could offer a great potential of being ideal transporting ions instead of Li ions.[8-10] Sodium ion batteries (SIBs) share similar rocking-chair mechanism with LIBs,[8] however, progress in this domain seems slow. The reason is likely attributed to distinctive electrochemical characteristics resulting from the large radius of Na ion (1.02 Å) when comparing with that of Li ion (0.76 Å).[11-13] More complex requirements for electrode materials' intrinsic properties to adapt the relatively large ion size often lead to unsatisfactory electrochemical performances, in particularly to rate capability that is even more critical due to the practical demand of charging/discharging in short time.

Rate capability depends on many different aspects of active materials, such as stability (both phase and morphology), ion diffusion, and electron transport. How to enable great rate capability without trading off high reversible capacity remains as a significant challenge,[14-18] in particular to Na-free transition metal oxide anode materials, whereas sodiated transition metal oxide cathode materials always possess

superior rate capabilities. A survey of literatures reveals the trend that much effort has been devoted to ameliorating rate capability through constructing various carbonaceous material-involved composites, such as activated carbon mixture,[15] surface carbon-coating,[19] graphene incorporation,[20] etc. An important issue of surface ion availability (i.e. the surface of materials can obtain enough ions from electrolyte for sodiation, including adsorption, reduction or insertion.) has been incredibly ignored for rate capability. Obviously, a sufficient amount of Na-ion supply is essentially required when anodes are operated at high rates. A possible reason for such ignorance might be substantial kinetic limitations arising from the larger size of Na ions that are not substantial enough or even don't exist in the counterpart situation of LIBs at low rates. For example, a recent study shows that less noteworthy intercalation of Na ions was observed in narrow amorphous TiO_2 nanotube array anodes because of the severely insufficient adsorption of Na ions on the electrode surface in aprotic electrolyte whereas strong adsorption of Li ions can be obtained under the same condition.[12, 21] Such observation highlights the fatal role of surface ion availability to the electrode surface, which is mainly determined by ion affinity and solvent wettability (penetration of the electrolyte). Li ions always exhibit high ion adsorption to the surface of electrode materials due to good ion affinity arising from small ion radius. However, with regard to Na ions, their ion affinity is not strong enough to voluntarily maintain a sufficient ion concentration at the surface,[12] then Na ions remain mainly in the bulk electrolyte and cannot screen the charge of electrons injected into the matrix. This deficiency would even worsen the

SIB performance at high-rate charging/discharging, where massive ions are required for the electrochemical processes. Fortunately, good solvent wettability is imperative for SIBs to enable the Na-ion availability to electrode surface through better penetration of the electrolyte and facilitate to establish sufficient ion concentration in the vicinity of the surface of active material during cycling, especially at high rates. Hence, we believe that good wettability of electrode surface to the electrolyte solution is significant to enhance the rate performance of SIBs.

The difficulties in observing the relationship between solvent wettability and rate performance in Na systems mainly stem from the serve demands of suitable material platform and structural model. On one hand, the material should meet the following two factors simultaneously. First, complicated mechanisms of Na storage, such as conversion or alloying/dealloying, should be avoided because deconstruction and rebuilding of atomic arrangement can largely change the surface properties of the materials. Second, the influences from particle shape/size, grain boundaries, facets and orientation on Na-adsorption, Na-ion diffusion and electron transport should be all excluded, so that we can focus on surface ion availability without the possible influences from material's characteristics. Accordingly, we choose amorphous TiO_2 (am-TiO_2) as a suitable material platform after striking a balance among various intrinsic features. The intercalation mechanism can be verified by the thermodynamic reversibility of Na intercalation reaction from the simulated atomic arrangement before and after Na-ion insertion (**Figure 1**). Meanwhile, amorphous hosts with

relatively high isotropy to effectively minimize all the afore-mentioned influences.[6,12,22-25] On the other hand, the wettability of a surface is associated outwardly with its roughness according to Wenzel model.[26] Beneficially from the much higher roughness homogeneously on microscale and nanoscale based on well-ordered colloidal crystal templates, inverse opal is a promising candidate of electrode architectures for improved solvent wettability comparing with planar films.[9] Overall, amorphous TiO_2 inverse opal is expected as a propitious model to solve the challenging point of low ion adsorption and further optimize the SIB rate capability.

In this work, amorphous TiO_2 inverse opal architecture was realized by colloid crystal template approach. Low-temperature atomic layer deposition (ALD) was used here to assist the fabrication processes in order to obtain the homogeneously rough surface on the nanoscale and clean surface. Based on this bridge, we overcome the obstacles of material platform and employ amorphous TiO_2 inverse opal as a prototype to illuminate a long-term-ignored kinetic factor: surface ion availability and its relationship with solvent wettability toward rate capacities. As a return for better solvent wettability, superior rate capabilities of SIBs are achieved within expectation in different types of electrolyte and different ion concentrations in electrolyte. According to the analysis of self-improvement processes and other electrochemical behaviours, the enhancement originates primarily from effective surface ion availability arising from good solvent wettability associated with well penetration of the electrolyte. In this regard, the attention on surface kinetic shows great significance

of ameliorating the SIB performance, especially at high rate. Our design opens up a promising avenue to design highly efficient electrodes for SIBs by adjusting the surface kinetic limitation and exerting the structural advantages. This understanding shall extend the design principle to some traditional electrodes for highly effective energy storage using other transport ions beside Li^+ and other storage mechanism.

2. Materials and methods

2.1. Materials.

All chemicals were purchased from Alfa Aesar GmBH & Co KG., and used without further purification

2.2. Fabrication of Polystyrene Spheres Colloidal Crystal Templates.

The well-ordered colloidal crystal templates comprising polystyrene spheres (PSs) with a face-centered cubic packing arrangement were fabricated using vertical deposition. Ti foils have been cleaned under sonication by sequentially immersing in acetone, ethanol and distilled water. The substrates were then immersed vertically in the 0.5 wt% polystyrene latex at 60 °C. The drying of sample at very low speed in the presence of moisture prevented the occurrence of cracking on the sample. As for the disordered PS template, the only difference is much faster evaporation rate.

2.3. Fabrication of amorphous TiO_2 architectures.

In a typical procedure, inverse opal amorphous TiO_2 were fabricated by low-temperature atomic layer deposition on the as-assembled colloidal crystal templates through a PicoSun SUNALETM R-150 ALD system (PicoSun, Finland). The reaction chamber was heated to 70°C, and $TiCl_4$ and H_2O were chosen as the precursors of Ti and O, respectively. $TiCl_4$ was pulsed for 0.1 s and purged for 10 s, followed by a 0.1 s pulse and 10 s purge of H_2O. This procedure was repeated for 600 cycles. For comparison, disordered porous and planar amorphous TiO_2 were also fabricated using the similar procedures on disordered PS template and Ti foil.

2.4. Preparation of P2-$Na_{2/3}Ni_{1/3}Mn_{2/3}O_2$.

Layered P2-$Na_{2/3}Ni_{1/3}Mn_{2/3}O_2$ was prepared by a co-precipitation method. $Ni(NO_3)_2$/$Mn(NO_3)_2$ with a stoichiometric ratio were mixed with sodium hydroxide. Na_2CO_3 was added later as the sodium source. Then the precursors were annealed at 600 °C for 4 h and 900 °C for 10 h in air.

2.5. Characterization.

X-ray diffraction (XRD) analysis was obtained from a SIEMENS/BRUKER D5000 X-ray diffractometer using Cu-Kα radiation at 40 kV and 40 mA, with the samples being scanned from 2θ = 20° - 80° at rate of 0.02° s^{-1} in a Bragg-Brentano geometry. Scanning electron microscopy (SEM) analysis was performed on a Hitachi S4800 field emission scanning microscopy. Transmission electron microscopy (TEM) analysis and selected area electron

diffraction (SAED) patterns were conducted by JEM-2010F (JEOL). X-ray photoelectron spectroscopy (XPS) measurements were recorded on a VG ESCALAB MK II X-ray photoelectron spectrometer with an exciting source of Mg Kα = 1253.6 eV. The binding energies obtained in the XPS spectral analysis were corrected for specimen charging by referencing C 1s to 284.5 eV. Raman spectra were detected by an inVia Raman microscope with a 514.5 nm Ar laser.

2.6. Electrochemical measurement.

The as-prepared various amorphous TiO_2 architectures were directly used as anodes without any conductive additive and polymeric binder. Electrochemical tests were performed through a coin cell configuration (CR2032) with a diameter and thickness of 20 mm and 3.2 mm, respectively, which were assembled in a nitrogen-filled glove box with oxygen and moisture concentrations kept below 0.1 ppm. Sodium metal foil used as a counter electrode was separated from the working electrode using a glass microfiber filter (Whatman, Grade GF/B) with the pore size of 1 μm. The electrolyte consists of 1 mol L^{-1} sodium perchlorate ($NaClO_4$) in propylene carbonate (PC, Aldrich anhydrous 99.7%). Cyclic voltammetry (CV) with different scan rates were recorded by a VSP electrochemical workstation (Bio-Logic, France) in the potential from 0.01 to 3.0 V (vs. Na/Na^+). Electrochemical impedance spectra (EIS) were also measured by a VSP electrochemical workstation (Bio-Logic,

France). All electrochemical studies were carried out at ambient temperature (20 ± 2 °C). For the reference, the electrolyte is changed into saturated $NaClO_4$ in PC and 1 mol L^{-1} $NaClO_4$ in ethylene carbonate and diethyl carbonate (volume ratio 1:1). The mass loading of IO, DOP and planar am-TiO_2 chosen in main text is 0.35, 0.2 and 0.04 mg cm^{-2}, respectively. Samples with higher mass loading are shown in supplementary material

With regard to the cathodes, they consist of 80% P2-$Na_{2/3}Ni_{1/3}Mn_{2/3}O_2$, 10% acetylene black, and 10% poly(vinylidene fluoride) (PVDF) by weight with an appropriate amount of 1-methyl-2-pyrrolidinone (NMP). The as-prepared mixture was pressed onto an aluminium foil with a subsequent drying at 120°C for 12 h in vacuum.

The coin batteries of full-cell were assembled under the same condition with half-cells of amorphous TiO_2 architectures. The counter electrodes could be the Na disk (half cell) and IO amorphous TiO_2 (full cell). To ensure a suitable positive-to-negative capacity ratio for cell balance, the mass ratio of active material for the cathode and anode is around 16. The potential window is set between 1.0 and 4.5 V.

2.7. Simulation of atomic arrangement of amorphous TiO_2 before and after Na intercalation.

The configuration of bulk amorphous TiO_2 with supercell dimensions of 2*2*3 was prepared using Molecular dynamics (MD) simulations. MD simulations

were carried out using Forcite module in Materials Studio software package using universal force field. The configuration of bulk amorphous TiO_2 with Na ion was prepared in similar way. The initial configuration of Na inserted TiO_2 was first created by adding Na atom into interstitial sites of amorphous TiO_2 randomly, then, subjected to geometric optimization using conjugate gradient algorithm.

3. Results

3.1. Fabrication and characterizations of amorphous TiO_2 inverse opal architecture.

The actualization of this tentative architecture requires facile and straightforward procedures. Here, we use colloidal crystal template method to accomplish the inverse opal scaffold.[27-32] **Figure 2a** outlines the typical two procedures of the general approach. Low-temperature atomic layer deposition is chosen as the infiltration technique considering its excellent conformability on a complex geometry and the features of polystyrene spheres (PSs). The details and reasons for choosing can be found in supporting information S1.

To validate this rational design, Figure 2c shows the representative scanning electron microscope (SEM) image of the inverse opal architecture, which is the replica translated from the periodic colloidal crystal opal template using PSs with ~500 nm diameter (Figure 2b). The top-view image demonstrates the high

degree of face-centered cubic colloidal orderliness where the close-packed (111) plane orients parallelly to the underlying Ti foil substrate. The cross-section image of final inverse opal architecture after reactive-ion etching (RIE) for 5 minutes is shown in inset of Figure 2c to identify the internal structural features. The throughout conformability further confirms the completely topologic transform from the opal PS template, so called inverse opal. It is clearly observed that the final architecture with a ~5.2 μm thickness consists of numerous close-packed "air spheres" separated by solid walls, where these well-defined hollow spheres on the top layer connect to the corresponding hollow spheres in the sub-layer through the channels. These open channels allow a bicontinuous inverse opal skeleton with a three-dimensionally interconnected pore system.[27,28,32] Transmission electron microscopic (TEM) images further indicate the periodic hollow structures arranged with hexagonal symmetry in both the center (Figure 2d) and the edge part (Figure 2e). The shell thickness of these hollow spheres is pretty uniform (~20 nm), which is well satisfied our expectation.

With regard to the phase of the as-prepared inverse opal architecture, the featureless selected area electron diffraction (SAED) pattern in Figure 2f indicates the amorphous nature, which is confirmed by the high-resolution TEM (HRTEM) image in Figure 2g as no discernible lattice fringe can be observed here. Other evidences, such as X-ray diffraction pattern (XRD, Figure

2h) and Raman spectra (Figure 2j), also verify the inexistent long-range ordering. A fact claimed more noteworthy is that two characteristic peaks located at 458.6 eV and 464.4 eV in X-ray photoelectron spectroscopy (XPS, Figure 2i) are assigned to +4 oxidation state arising from $2p_{3/2}$ and $2p_{1/2}$ signal, suggesting that Ti ions are mainly presented as Ti^{4+} in the lattice.[33] Moreover, after annealing at 350 °C, the phase can convert completely to anatase TiO_2 as certified by XRD pattern (**Figure S1**). In this sense, we realize the rational design of the am-TiO_2 inverse opal architecture, where no carbon is contained in the architecture in accord with the Raman spectrum ranging from 1200 to 1800 cm^{-1}.[34]

3.2. Electrochemical characteristics of amorphous TiO_2 inverse opal architecture.

As mentioned before, the ion surface availability in SIBs is different from that in LIBs due to the poorer affinity of transporting ions to the surface of TiO_2,[4b] so that the solvent wettability (*i.e.* penetration of the electrolyte) is significant for the SIB performance, especially at high rates. To validate our hypothesis, two-electrode coin cells with amorphous TiO_2-based working electrodes were employed as presented in **Figure 3a**. For comparison, we analyze the SIB performance of two reference anodes: disordered porous (DOP) am-TiO_2 formed from disordered colloidal template and planar am-TiO_2, which were also directly fabricated on Ti foil with the same ALD processes as those of IO

am-TiO_2, to illuminate the detailed influences of solvent wettability for SIB performance. Corresponding characterizations exhibited in **Figure S2-S3** also indicate the amorphous nature and purity of +4 oxidation state with different morphologies.

Successful implementation of our designed configuration can produce excellent SIB performance. Figure 3b shows the cycling performance of three architectures directly employed as working electrodes by galvanostatic charge and discharge between 0.01 and 3.0 V (*vs.* Na/Na^+) at the current density of 50 mA g^{-1}. The corresponding sodiation voltage profiles of different cycles are displayed in Figure 3d-3e (2^{nd}, 20^{th}, 100^{th} cycles) and **Figure S4** (1^{st} cycle) to see decay of the electrodes more clearly. Since the Ti foil as the substrate provides little contribution for the final capacity (**Figure S5**), all of results confirm the electrochemical reversibility of Na ions within amorphous TiO_2. IO am-TiO_2 stands out with its high capacities after long cycling. It is worth noting that the first discharge capacity is around 704 mA h g^{-1}, whereas those of DOP and planar am-TiO_2 are only 333 and 182 mA h g^{-1}, respectively. Being consistent with rather low initial columbic efficiency (CE), the much higher irreversible capacities is presumably associated with the formation of the solid-electrolyte-interface (SEI) layer at the surface of active material, hinting at much larger surface area deriving from the complex inverse opal architectures. Moreover, the large surface sodium storage also contributes some

capacities, so that at the initial stage, the capacities slightly exceed the theoretical capacity of Na-ion intercalation reaction (~335 mAh g^{-1}). With gradually increased CE (over 90% since the 19th cycle) upon continuous cycling, the interfacial processes that result in unusually high first capacities has been completed. Even upon 100 cycles, the specific capacity of IO am-TiO_2 anode still remain ~203 mA h g^{-1}, whereas DOP and planar anodes deliver significantly lower capacities of ~126 and 147 mA h g^{-1}, respectively. This value represents the highest specific capacity within various pure TiO_2 anodes[35-43] and is even higher or comparable to composite TiO_2 systems.[44-45] The detailed comparison with previously reported TiO_2-based anodes can be seen in **Table S1**. As discussed at the beginning, one key advantage of the architecture design is that it may enable high capacity and high power on one material at the same time. To examine this potential, the rate capabilities of the am-TiO_2 in Figure 3c and corresponding charge/discharge curves in **Figure S6** are also evaluated to investigate the feasibility for high power application. It is the first report on amorphous TiO_2 anodes with outstanding rate performance. Even cycled at a current density as high as 5000 mA g^{-1}, we can still obtain a specific capacity of ~113 mA h g^{-1}, which is 1.3-fold and 2.4-fold higher than those of DOP and planar am-TiO_2. Noteworthy, the ratio is only 1.2 and 1.5 under 50 mA h g^{-1}, indicating that the specific capacities of planar anode drop more quickly with the charge rate increased. After cycling at high rates, the IO anode exhibits a recovered specific

capacity of ~239 mA h g^{-1} when the current density is switched back to 50 mA g^{-1}. To the best of our knowledge, the high-rate capacities of IO am-TiO_2 are also much better than those in other literatures as evaluated in **Figure S7**. As well known, high rate operation is an important challenge for SIBs because of difficulties in insertion and extraction of the large Na ions into the host lattice. Much ongoing studies are focus on meeting this challenge through constructing heterostructures to improve the electron/ion diffusion, such as carbon-based composites (carbon-coated TiO_2 nanorods,[34] carbon-coated TiO_2 nanoparticles,[36] carbon-coated TiO_2 microspheres,[45] and TiO_2 nanoparticles/graphene composites[20,46]). However, comparing with previous literatures, it is worth emphasizing that the above reported great capabilities are achieved by incorporating carbonaceous materials as either conductive additive, binder or coating layer, whereas our electrodes don't contain any kind of such materials. Moreover, during the fabrication processes, the crystalline electrodes always undergo annealing process to achieve the fixed atomic arrangement, but as for the amorphous TiO_2, heat treatment is completely not necessary, which makes the fabrication more feasible and low-cost.

3.3. Observation of self-improving process.

There have been reports that increased concentration of interfacial regions in amorphous materials may facilitate the ionic diffusion by forming percolation pathways. It inspires us to explore the detailed kinetic factors associated with

the surface to illuminate the merit of IO am-TiO_2. Therefore, we next seek to survey the electrochemical behaves upon long charge/discharge in Figure 3b and 3c. Looking carefully into the curves, we find that the specific capacities of IO and DOP am-TiO_2 slightly decrease along with cycles like most reported electrodes, however, the specific capacities of planar am-TiO_2 undergo a self-improving trend, which can also be observed from the curves of other electrodes in SIBs, such as amorphous TiO_2 nanotubes,[12,22] anatase TiO_2 nanocubes,[37] amorphous $FePO_4$ nanosphere,[25] etc. Furthermore, the self-improving process tends to be prolonged with increased rates. As shown in **Figure 4d**, the specific capacities of planar am-TiO_2 keep increasing until the 105^{th} cycle at 50 mA g^{-1}, while the specific capacities stop increasing at the 370^{th} and 405^{th} cycle at the current density as fast as 500 and 2000 mA g^{-1}, respectively. With regard to DOP am-TiO_2 which possesses no self-improving capacities at 50 mA g^{-1}, the specific capacities also remain increasing until 14^{th} and 19^{th} cycles when the rate increases to 500 and 2000 mA g^{-1}. But for IO am-TiO_2, the specific capacities increase only at the first 4 cycles at a fast rate of 2000 mA g^{-1}, allowing full utilization of materials at initial stage. The SEM images after cycles (**Figure S8b-S8d**) also confirm the overall integrity of complex porous architectures from the preserved morphology on the current collector, while that of planar am-TiO_2 is completely destroyed. So it is impossible that the fast capacities fading resulted from structural collapse would cover the fact of self-improving capacities upon cycling. According to

the previous literatures, the self-improvement of the specific capacities sometimes occurs at fast cycling in LIBs.[12] Several competing mechanisms might be used to explain the observed differences. Some studies conclude that the origin of the self-improving stage is attributed to the electrochemically driven phase transformation.[46] However, we cannot observe any extra peak from the XRD patterns of these anodes collected after 100 discharge/charge cycles (Figure S8a), indicating the consistent amorphous phase. Another mechanism mentioned before is that the self-improvement of capacities stands as an active process. These simple curves cannot answer the questions about the loose concept, such as: Why does the active process happen? What enables the self-improvement stage?

To illuminate the origins, cyclic voltammetry (CV) curves may serve as a powerful tool to investigate the detailed electrochemical processes. As shown in Figure 4g-4i are CV curves of the 1^{st}, 2^{nd}, 5^{th} and 10^{th} cycle at a scan rate of 0.1 mV s^{-1} in the potential range of 0.01-3.0 V (*vs.* Na/Na^{+}) of IO, DOP and planar am-TiO_2, respectively, and the corresponding structural features of the electrodes are instructed in Figure 4a-4c. All the curves share similar appearances, indicating that Na-ion insertion/extraction in the three samples are all tied to the broad energy dispersion of the sodiation sites.[15,47] Although following the similar general trend, as pointed by the arrays in Figure 4i, planar anode shows a slower stability rate as is seen from the more obvious

differences from the 2^{nd} and the $5^{th}/10^{th}$ cycle than those of IO and DOP am-TiO_2 through the whole voltage range. In other words, planar anode needs a longer active process, which is completely invisible for IO and DOP am-TiO_2. Aside from the CV spectra, voltage profiles in Figure 3d-3f reveal more details about the electrochemistry of sodiation/desodiation in the host to see if this active process is necessary for the IO and DOP am-TiO_2. Since the first discharge process for all three anodes result more from the continuous formation of SEI layer (Figure S4), we only list the charge/discharge voltage profiles of 2^{nd}, 20^{th} and 100^{th} cycles at 50 mA g^{-1} with the colours ranging from dark to light. From the shape of charge/discharge curves and irreversible specific capacities, we also infer that the electrochemical reaction is related to the intercalation reaction together with surface charge storage. In accordance with CV data, the specific capacities of IO and DOP am-TiO_2 show a slightly decreased trend throughout the whole voltage range. On the contrary, specific capacities of planar anode turn into increasing trend upon cycling, especially from 1.5 V to 0.2 V. Choosing the capacities of different cycles at 0.8 V *vs.* Na/Na^+ for an example, corresponding trend of capacity evolution can be clearly observed from the inset figures in Figure 3d-3f. The discharge curves in **Figure 5a-5f** mirror the trend that self-improving processes will be prolonged at high rates, which should also be attributed to the different electrochemical behaves for sodiation.

4. Discussion

To deeply understand the relationship between self-improving process and superior rate performance, here, four important points should be first predeclared and emphasized considering the electrochemical measurement of IO, DOP and planar am-TiO_2. (i) According to the Raman spectra in **Figure** 2i and **S9**, no peaks assigned to the signals of carbon can be investigated from 1200 cm^{-1} to 1800 cm^{-1}. All the three samples don't contain any carbon materials that can alter the long-term stability and rate performance,[48] and thus the whole improvements should be attributed to the active materials themselves (both intrinsic properties and architecture engineering). (ii) The effects from intrinsic features of crystalline materials (particle shape/size, grain boundaries, facets and orientation, etc.) during various electrochemical processes, like Na-adsorption/insertion and electron/ion diffusion, can be all excluded because of relatively high isotropy of amorphous TiO_2. (iii) The thickness of the building blocks is uniform owing to the concise deposition control using ALD. So the length of ion diffusion keeps the same. (iv) All the three samples are stored in N_2 before measurement. So we can exclude the detrimental influences from adsorption and/or adhesion of water molecular (H_2O) on the surface. (v) As for the electron transport paths, it is clear that planar sample possesses the shortest one, which should be benefit for the SIB

performance, yet the rate capacities of planar am-TiO_2 are much poorer than those of porous samples. Corresponding charge transfer resistance calculated from electrochemical impedance spectroscopy (EIS) measurements (**Figure S10**) can further prove the easier charge transfer of IO and DOP am-TiO_2, which contribute to better capacities.

With this understanding established, the debatable results drive us to look for the reasons from surface kinetic factors because the fact that distinguishes the three anodes from each other is the different structural features and corresponding solvent wettability. In the case of the poor affinity to the TiO_2 surface in aprotic electrolyte,[12,13] a relatively high concentration of Na ions need to first be established near the surface, then Na ions can concentrate at reduced Ti centers, and finally diffuse into the TiO_2 matrix. Insufficient ion availability near the surface can account for observed improvement of the capacity upon cycling.[13] Furthermore, with the rate increasing, the critical concentration of Na ions at the surface which is established through electrostatic attraction is increasing correspondingly, and thus a longer self-improving process is necessary to build up higher ion concentration as required. Considering the surface storage and intercalation mechanism, which has been proved by the simulation in Figure 1, the analysis of XPS spectra after discharge (**Figure S11**) and *b*-value based on the CV curves at different rates (**Figure S12**), the surface ion availability should play a more essential role on

providing enough Na ions inserted into the am-TiO_2 matrix, i.e. the capacity. As well known, the contact chance between ions and active materials depends on the ion concentration and penetration of electrolyte. With regard to the former factor, the most popular propylene carbonate electrolyte with saturated sodium perchlorate ($NaClO_4$) is used as another electrolyte to show the effects of active ion concentration. The discharge capacities upon cycling in 2000 mA g^{-1} shown in **Figure S13** completely mirror the trend of self-improvement processes in common electrolyte, suggesting that the ion concentration in electrolyte is not the decisive factor here.

As for penetration of electrolyte, solvent wettability measured by the contact angle is a vital parameter to provide an indication of how effectively a liquid will spread over a surface. Shown in **Figure 6a-6c** is the contact angles of the three architectures. Obvious differences evidence distinct solvent wettability. The contact angle of IO am-TiO_2 for the electrolyte is only ~17.4 °, which is much smaller than DOP (28.0 °) and planar (47.2 °) am-TiO_2. It is worth noting that the contact angel can be adjusted by surface roughness for a certain material according to the Wenzel model as following[26,49]

$$\cos \theta^* = r \cos \theta$$

where θ^* is the apparent contact angle. θ is the contact angle of a planar film with smooth surface. r is the roughness ratio defined as the ratio of true area of the surface to the projected area on the horizontal plane. This equation hints at

the fact that the solvent wettability can be enhanced by increasing the surface roughness. Assuming that planar am-TiO_2 possesses a completely smooth surface, the roughness of IO am-TiO_2 is calculated to be 1.4, which is closed to the theoretical value (The detailed calculation can be found in **Figure S14**).

On account of their high roughness ratio r as diagrammed in Figure 6, the periodic micro/nanostructured arrays templated by PSs should be attributed to smaller contact angle and further induce extreme solvent wettability on the surface. A larger number of Na ions therefore are available to establish sufficient ion concentration to support cycling. Not only at the surface, such a bicontinuous architecture permits the transport of Na ions throughout the inner skeleton while also providing a continuous path in the pore system that can allow complete penetration of the electrolytes. The macropores interconnect with each other form open-edge geometry to contain more electrolytes. The inner surface with high roughness also improves the solvent wettability and Na-ion accessibility. Moreover, upon repeating charge/discharge processes, IO am-TiO_2 with integrity originated from the robust interconnected network can keep the enough concentration of Na ions to support long cycles, especially at high rates. Slight decreasing with cycling is attributed to the intrinsic features of am-TiO_2. As a result of these structural advantages, electrodes for Na insertion/deinsertion display great rate capacities. As for planar architecture, relatively low Na-ion concentration results in self-improving capacities in SIBs

at a slower rate as Na ion concentration is building up with the cycling proceeds and structure collapse (Figure S8d), *i.e.* the active process. If the cycling rate is higher, more and more Na ions are necessary to support the fast cycling, leading to longer self-improving processes. This conclusion can also be proved by the mass of intercalated Na ions after the 10 cycles (**Figure S15**). To rule out the possible influences of electrolyte type, instead of widely-used propylene carbonate, we take another electrolyte consisted of 1 mol L^{-1} $NaClO_4$ in ethylene carbonate and diethyl carbonate (volume ratio 1:1) as an example. As shown in **Figure 7**, better solvent wettability is beneficial for the improved rate performance in virtue of better ion availability through facile penetration of electrolyte according to the similar analysis of self- improvement processes.

To display the feasibility of IO am-TiO_2 anode in practical applications, a narrow potential window is expected to achieve required capacities. In general, the potential window relevant for anodes should be 0.05 - 1.8 V *vs.* Na/Na^+. Capacities measured below 0.05 V may relate to sodium deposition which is dangerous, while capacities measured > 1.8 V are not relevant for anode materials. Hence, we re-calculate the capacities of IO, DOP and planar am-TiO_2 at 50, 500 and 2000 mA g^{-1}. Corresponding realistic capacities are displayed in **Figure 8** (light column) compared with the original capacities based on the potential window of 0.01 - 3.0 V (dark column). It is clear to find that capacities measured between 1.8 V and 50 mV contribute most to overall

capacities. The capacities measured between 0.05 and 1.8 V are still comparable to the best results of TiO_2-based sodium batteries.[33-43]

Furthermore, in order to check the potential of IO am-TiO_2 anode in full cells, we chose layered P2-$Na_{2/3}Ni_{1/3}Mn_{2/3}O_2$, a sodiated transition metal oxide material, as cathode to assemble the full cell together with IO am-TiO_2 anode. Corresponding characterization and electrochemical performance can be found in **Figure S16 - S17**.

As shown in cycling performance in **Figure 9a-9c**, the full cells show a long-term stability and large sodium storage. A capacity of ~189.2 mAh g^{-1} (with respect to the mass of anode) can be obtained even after 100 cycles at 50 mA g^{-1}, while ~86.7 mAh g^{-1} after 500 cycles at 500 mA g^{-1}. The capacity retentions are pretty good, which is more attractive in practical application. Moreover, it is clearly observed from Figure 9d that rate capabilities of this full cell is also good even at current density as high as 5000 mA g^{-1}, and these capacities can be fully recovered when the current density is switched back to 50 mA g^{-1}. These results of full cells evidence the possibility of employing IO am-TiO_2 anodes to build high energy storage devices.

Furthermore, practical loading is important for large scale applications. Keeping this point in mind, besides the proof-of-concept demonstration example to illuminate the possibility of amorphous TiO_2 as anodes, we could further improve the mass loading *via* adjusting the morphology diameters, such

as increasing the ratio of wall thickness to diameter of hollow spheres that directly depends on the diameter of the used PSs and increasing the overall thickness of active materials. Detailed discussions could be found in **Figure S18**. Superior rate performance (**Figure S19c**) could be achieved with inverse opal with higher mass loading (Figure S18a-S18b).

Based on the comprehensive consideration, we contribute better rate performance of SIBs mainly to the sufficient surface ion availability arising from good solvent wettability and penetration of electrolyte. Yet there is still room for improvement in the future. With the roles of am-TiO_2 in the nanostructure understood and experimental parameters fixed on rate performance, such as, further optimizing the pore size to accelerate electron/ion transport. The large first-cycle irreversible capacities for the IO sample are always undesirable in full Na-ion cells. The possible ways to overcome this problem could be centred on alleviating the influences of solid-electrolyte-interface (SEI) layer and polarization, such as changing the electrolyte to make a stable SEI layer, design of heterostructures, intrinsic structural engineering, etc. On the other hand, an ideal anode should possess narrow potential window to achieve the required capacities for practical applications, especially at low potential range like carbon. Further shortening the potential window and enlarging the operation potential range in full cells are vital for practical applications, and could be realized by intrinsic structural

engineering and optimizing the kinetic factors. Though the relative study is beyond our present work, we are looking forward to more effort for these open questions in the near future.

5. Conclusion

Inverse opal amorphous TiO_2 architecture is achieved for the first time to meet the challenging point of low ion adsorption for sodium battery. Within expectation, such an anode provides superior specific capacities and high-rate performance among various TiO_2 anodes, and even higher or comparable to the component anodes. The retained capacity after 100 cycles at 50 mA g^{-1} can reach ~203 mA h g^{-1}, and even at the current density as high as 5000 mA g^{-1}, a capacity of ~113 mA h g^{-1} can be obtained with almost recovering the low rate capacity. Due to the relatively high isotropy of am-TiO_2 lattices, this anode serves as an ideal platform to observe the relationship between surface ion availability and the SIBs performances through the bridge of solvent wettability. We can attribute the enhancement primarily to effective surface ion availability resulting from good solvent wettability by increasing the roughness of the electrode surface, which is proved by the contact angle measurement and the analysis of sodiation/desodiation profiles. All the results highlight the positive effects of the optimizing surface kinetic factors, which unambiguously confirm the high dependence of electrochemical performances on superior

electrode design. Our finding facilitates the feasible development of intercalation electrodes for various secondary ion batteries, especially with large transport ions.

Acknowledgements

This work was financially supported by European Research Council (ThreeDsurface, 240144), European Research Council (HiNaPc, 737616), BMBF (ZIK-3DNanoDevice, 03Z1MN11), German Research Foundation (DFG: LE 2249_4-1). Dr. M. Zhou and Dr. Y. Xu contributed equally to this work.

Appendix A. Supplementary material

Supplementary data associated with this article can be found in the online version at http://….

Appendix B. Figures and caption

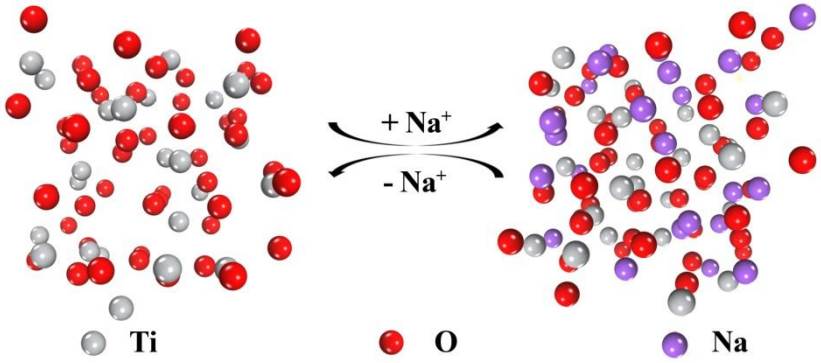

Figure 1. Schematic simulation of atomic arrangement of amorphous TiO_2 before and after Na ion insertion. (a) Amorphous hosts, (b) Na-ion insertion in amorphous hosts.

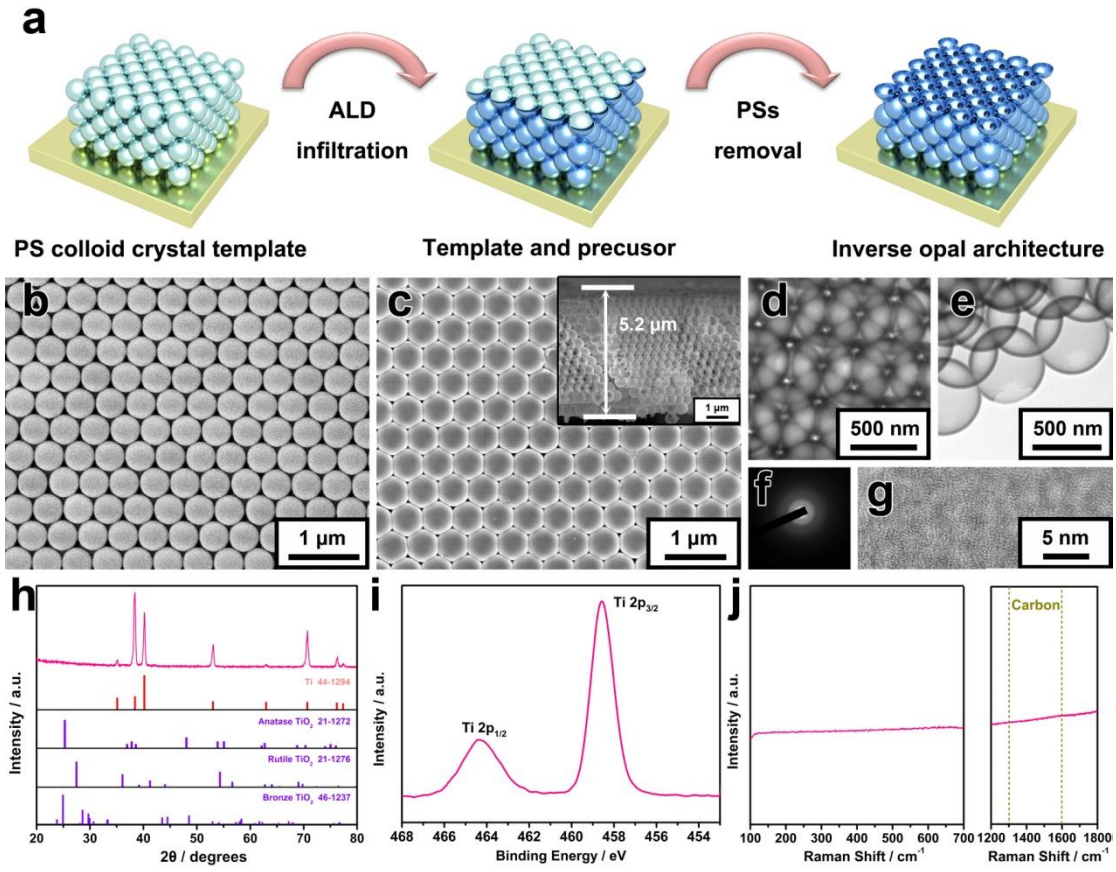

Figure 2. Fabrication illustration and characterizations of inverse opal am-TiO_2 architecture. (a) Schematic illustration of the fabrication processes. To illuminate the inner details, half of the top layer is peeled off in the scheme. (b, c) Typical SEM

images of colloidal crystal template of 500 nm PSs (b) and corresponding inverse opal architecture (c) with crossing section view inset; (d-f) Typical TEM images of inverse opal architecture in center part (d), edge part (e); (f) Typical SAED pattern of (d); (g) HRTEM image of part of (d); (h) XRD pattern, (i) XPS data, (j) Raman spectra.

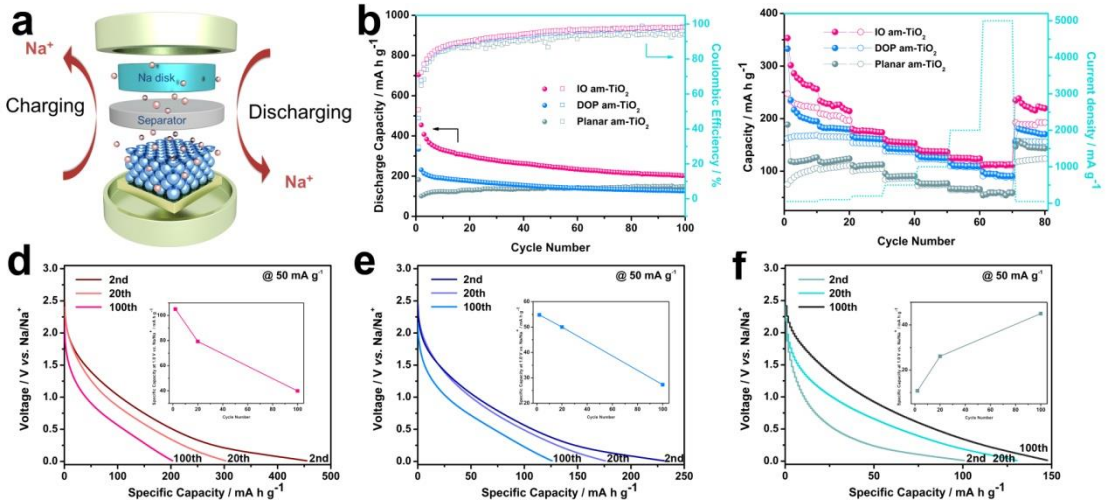

Figure 3. Electrochemical properties of various am-TiO_2 architectures. (a) Scheme of a two-electrode 2032-type coin cell with am-TiO_2 as anode and sodium disk as cathode. (b) Cycling performance of the anodes at the rate of 50 mA g^{-1}. (c) Rate capability of the anodes. (d-f) Sodiation voltage profiles at 50 mA g^{-1} (d) IO am-TiO_2, (e) DOP am-TiO_2 and (f) planar am-TiO_2.

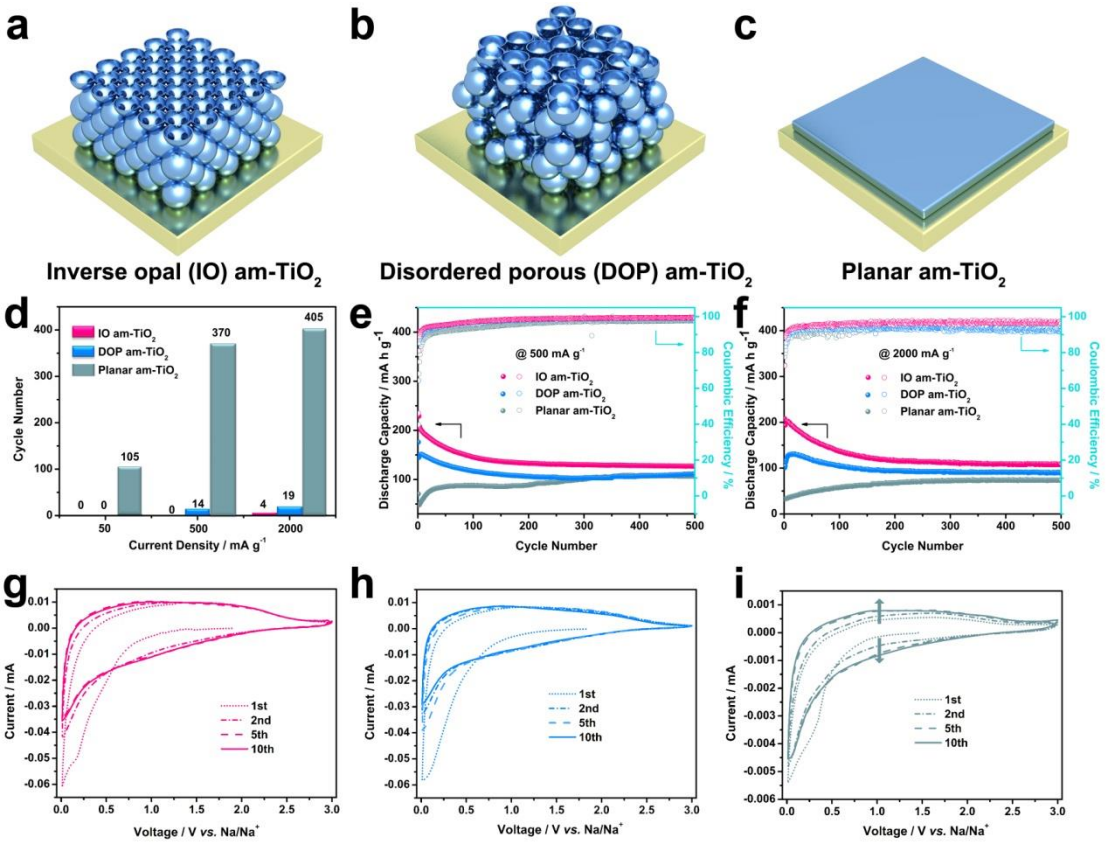

Figure 4. Electrochemical properties of various amouphous TiO_2 at different rates. (a-c) Scheme of the structural features of three different architectures; (d) The numbers of self-improving process of IO, DOP and planar am-TiO_2; The comparison of discharge capacity and coulombic efficiency of IO, DOP and planar am-TiO_2 at (e) 500 mA g^{-1}, (f) 2000 mA g^{-1}; (g-i) the CV curves at a scan rate of 0.1 mV s^{-1} in the potential range of 0.01-3.0 V of three different architectures.

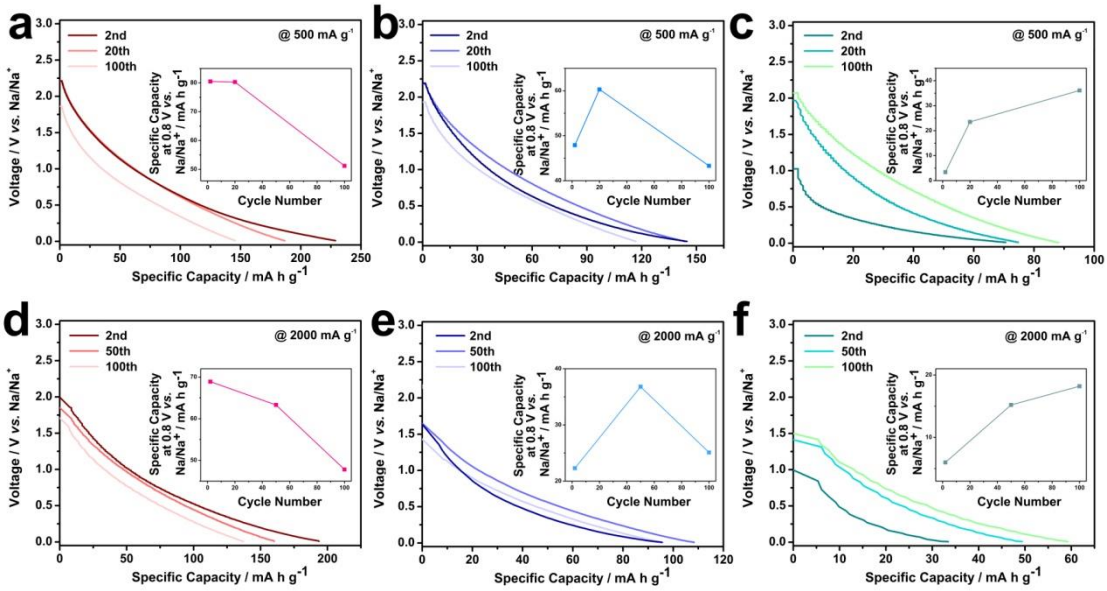

Figure 5. Self-improving processes at different rates. Sodiation voltage profiles at 500 mA g^{-1} and 2000 mA g^{-1} of (a, d) IO am-TiO_2, (b, e) DOP am-TiO_2 and (c, f) planar am-TiO_2. Insets show corresponding trend of capacity evolution of different cycles at 0.8 V vs. Na/Na^+.

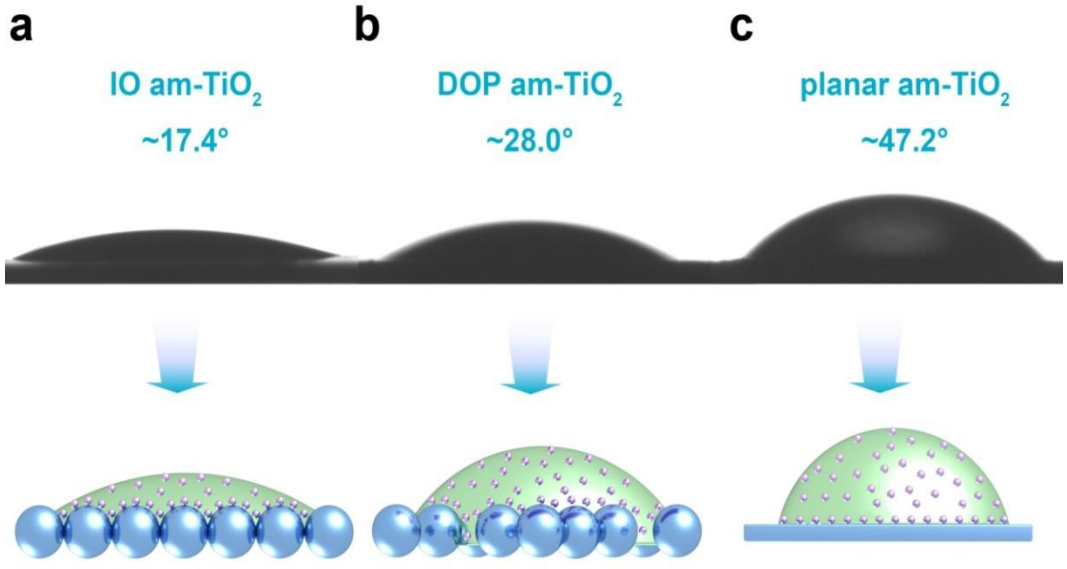

Figure 6. The solvent wettability of various amorphous TiO_2 architectures. The shape of electrolyte droplets on the surface of different architectures and corresponding ideal schematic representation: (a) inverse opal am-TiO_2; (b) disordered porous am-TiO_2; (c) planar am-TiO_2.

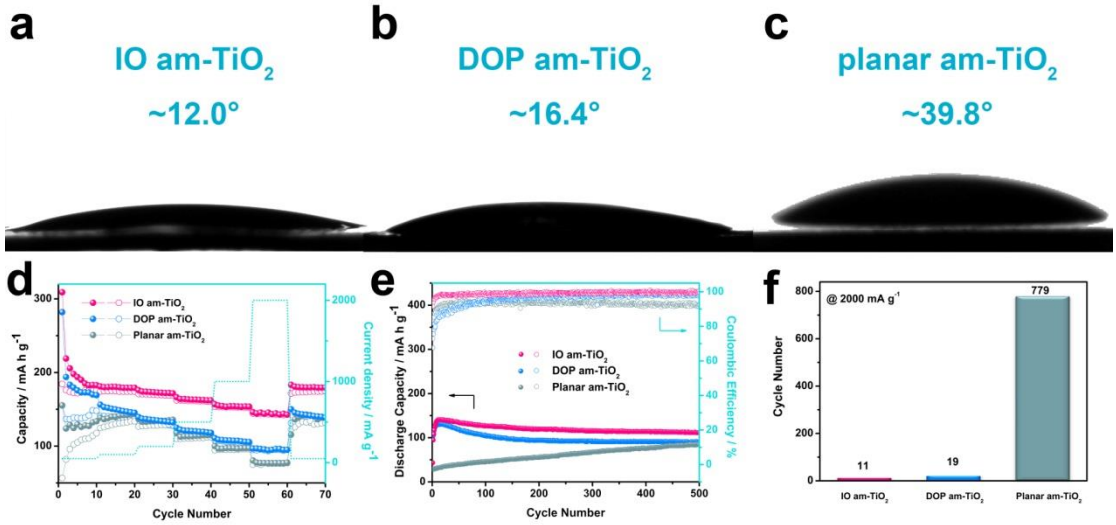

Figure 7. The solvent wettability and SIB performance of various amorphous TiO_2 architectures in the electrolyte with 1 mol L^{-1} $NaClO_4$ in ethylene carbonate and diethyl carbonate (volume ratio 1:1). (a-c) The shape of electrolyte droplets on the surface: (a) inverse opal am-TiO_2; (b) disordered porous am-TiO_2; (c) planar am-TiO_2. (d) The numbers of self-improving process of IO, DOP and planar am-TiO_2 anodes; (e, f) The comparison of discharge capacity, columbic efficiency and self-improvement processes of IO, DOP and planar am-TiO_2 anodes at 2000 mA g^{-1}.

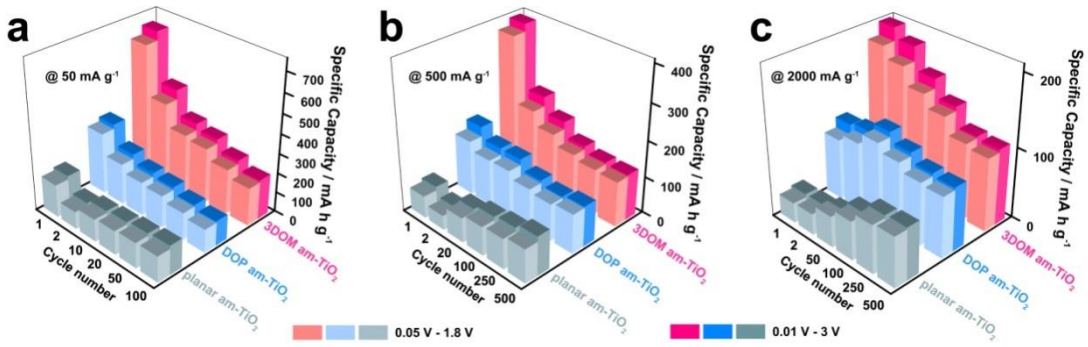

Figure 8. The discharge capacities of IO, DOP and planar am-TiO_2 measured with different potential window at various rates: (a) 50 mA g^{-1}, (b) 500 mA g^{-1}, (c) 2000 mA g^{-1}.

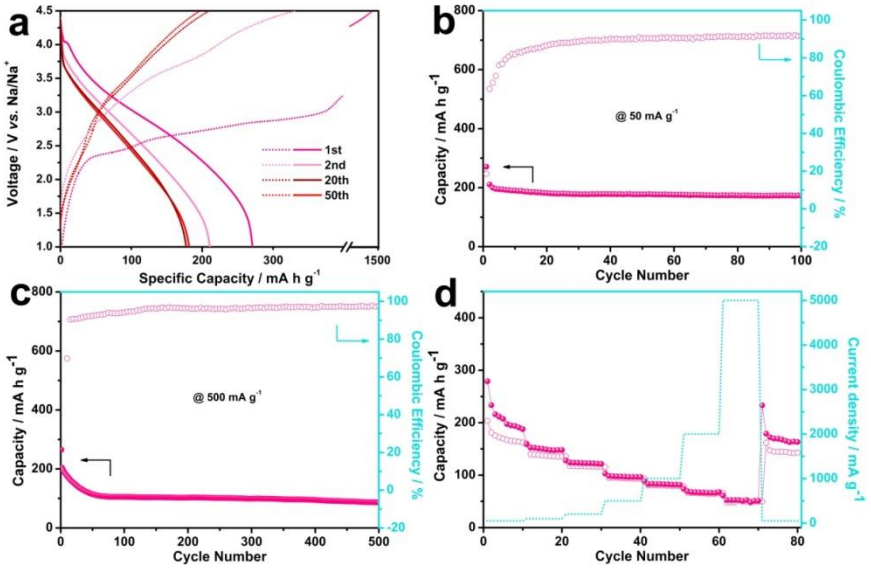

Figure 9. Electrochemical performance of a full cell consisted of P2-$Na_{2/3}Ni_{1/3}Mn_{2/3}O_2$ cathode and inverse opal am-TiO_2 anode. (a) Galvanostatic charge/discharge voltage profiles of 1st, 2nd, 20st, 50st cycles, (b) Cycling performance at a current density of 50 mA g^{-1} (relative to the anode weight), (c) Cycling performance at a current density of 500 mA g^{-1} (relative to the anode weight), (d) Rate capability (with respect to the anode weight).

Reference

[1] B. Dunn, H. Kamath, J.-M. Tarascon Science 334 (2011) 928-935.

[2] Z. Yang, J. Zhang, M. C. W. Kintner-Meyer, X. Lu, D. Choi, J. P. Lemmon, J. Liu Chem. Rev. 111 (2011) 3577-3613.

[3] Y. Xu, M. Zhou, Y. Lei, Adv. Energy Mater. 6 (2016) 1502514.

[4] M.-C. Lin, M. Gong, B. Lu, Y. Wu, D.-Y. Wang, M. Guan, M. Angell, C. Chen, J. Yang, B.-J. Hwang, H. Dai Nature 520 (2015) 324-328.

[5] S. Zhou, X. Yang, J. Xie, Z. I. Simpson, D. Wang Chem. Comm. 49 (2013) 6470-6476.

[6] V. Mathew, S. Kim, J. Kang, J. Gim, J. Song, J. P. Baboo, W. Park, D. Ahn, J. Han, L. Gu, Y. Wang, Y.-S. Hu, Y.-K. Sun, J. Kim NPG Asia Mater 6 (2014) e138.

[7] A. K. Padhi, K. S. Nanjundaswamy, J. B. Goodenough J. Electrochem. Soc. 144 (1997) 1188-1194.

[8] V. Palomares, P. Serras, I. Villaluenga, K. B. Hueso, J. Carretero-Gonzalez, T. Rojo Energy Environmental Sci. 5 (2012) 5884-5901.

[9] N. Yabuuchi, M. Kajiyama, J. Iwatate, H. Nishikawa, S. Hitomi, R. Okuyama, R. Usui, Y. Yamada, S. Komaba Nat. Mater. 11 (2012) 512-517.

[10] P. Barpanda, G. Oyama, S.-i. Nishimura, S.-C. Chung, A. Yamada Nat. Commun. 5 (2014)

[11] J. Qian, X. Wu, Y. Cao, X. Ai, H. Yang Angew. Chem. Int. Ed. 52 (2013) 4633-4636.

[12] H. Xiong, M. D. Slater, M. Balasubramanian, C. S. Johnson, T. Rajh J. Phys. Chem. Lett. 2 (2011) 2560-2565.

[13] R. Shannon Acta Crystallogr. Sect. A 32 (1976) 751-767.

[14] N. Yabuuchi, K. Kubota, M. Dahbi, S. Komaba Chem. Rev. 114 (2014) 11636-11682.

[15] M. D. Slater, D. Kim, E. Lee, C. S. Johnson Adv. Funct. Mater. 23 (2013) 947-958.

[16] J. Wang, X. Sun Energy Environ. Sci. 8 (2015) 1110-1138.

[17] C. Wang, Y. Xu, Y. Fang, M. Zhou, L. Liang, S. Singh, H. Zhao, A. Schober, Y. Lei J. Am. Chem. Soc. 137 (2015) 3124-3130.

[18] Y. Xu, M. Zhou, X. Wang, C. Wang, L. Liang, F. Grote, M. Wu, Y. Mi, Y. Lei Angew. Chem. Int. Ed. 54 (2015) 8768-8771.

[19] D.-Y. Park, S.-T. Myung ACS Appl. Mater. Interfaces 6 (2014) 11749-11757.

[20] H. A. Cha, H. M. Jeong, J. K. Kang J. Mater. Chem. A 2 (2014) 5182-5186.

[21] B. Enright, G. Redmond, D. Fitzmaurice J. Phys. Chem. 98 (1994) 6195-6200.

[22] Z. Bi, M. P. Paranthaman, P. A. Menchhofer, R. R. Dehoff, C. A. Bridges, M. Chi, B. Guo, X.-G. Sun, S. Dai J. Power Sources 222 (2013) 461-466.

[23] E. Uchaker, Y. Z. Zheng, S. Li, S. L. Candelaria, S. Hu, G. Z. Cao J. Mater. Chem. A 2 (2014) 18208-18214.

[24] G. Venkatesh, V. Pralong, O. I. Lebedev, V. Caignaert, P. Bazin, B. Raveau Electro. Comm. 40 (2014) 100-102.

[25] Y. Fang, L. Xiao, J. Qian, X. Ai, H. Yang, Y. Cao Nano Lett. 14 (2014) 3539-3543.

[26] Y. Li, G. Duan, G. Liu, W. Cai Chem. Soc. Rev. 42 (2013) 3614-3627.

[27] J. S. Sakamoto, B. Dunn J. Mater. Chem. 12 (2002) 2859-2861.

[28] M. Zhou, H. B. Wu, J. Bao, L. Liang, X. W. Lou, Y. Xie Angew. Chem. Int. Ed. 52 (2013) 8579-8583.

[29] M. Zhou, J. Bao, M. Tao, R. Zhu, Y. Lin, X. Zhang, Y. Xie Chem. Comm. 49 (2013) 6021-6023.

[30] M. Zhou, J. Bao, Y. Xu, J. Zhang, J. Xie, M. Guan, C. Wang, L. Wen, Y. Lei, Y. Xie ACS Nano 8 (2014) 7088-7098.

[31] L. Wen, M. Zhou, C. Wang, Y. Mi, Y. Lei, Adv. Energy Mater. (2016) 1600468

[32] M. Zhou, Y. Xu, J. Xiang, C. Wang, L. Liang, L. Wen, Y. Fang, Y. Mi, Y. Lei, Adv. Energy Mater. (2016) 1600448

[33] B. Erdem, R. A. Hunsicker, G. W. Simmons, E. D. Sudol, V. L. Dimonie, M. S. El-Aasser Langmuir 17 (2001) 2664-2669.

[34] K.-T. Kim, G. Ali, K. Y. Chung, C. S. Yoon, H. Yashiro, Y.-K. Sun, J. Lu, K. Amine, S.-T. Myung Nano Lett. 14 (2014) 416-422.

[35] Y. Xu, E. Memarzadeh Lotfabad, H. Wang, B. Farbod, Z. Xu, A. Kohandehghan, D. Mitlin Chem. Comm. 49 (2013) 8973-8975.

[36] L. Wu, D. Buchholz, D. Bresser, L. Gomes Chagas, S. Passerini J. Power Sources 251 (2014) 379-385.

[37] L. Wu, D. Bresser, D. Buchholz, S. Passerini J. Electro. Soc. 162 (2015) A3052-A3058.

[38] X. Yang, C. Wang, Y. Yang, Y. Zhang, X. Jia, J. Chen, X. Ji J. Mater. Chem. A 3 (2015) 8800-8807.

[39] J. C. Perez-Flores, C. Baehtz, A. Kuhn, F. Garcia-Alvarado J. Mater. Chem. A 2 (2014) 1825-1833.

[40] L. Wu, D. Bresser, D. Buchholz, G.A. Giffin, C.R. Castro, A. Ochel, S. Passerini, Adv. Energy Mater. 5 (2015) 1401142.

[41] J. P. Huang, D. D. Yuan, H. Z. Zhang, Y. L. Cao, G. R. Li, H. X. Yang, X. P. Gao RSC Adv. 3 (2013) 12593-12597.

[42] C. Chen, Y. Wen, X. Hu, X. Ji, M. Yan, L. Mai, P. Hu, B. Shan, Y. Huang Nat. Commun. 6 (2015) 6929.

[43] J.R. Gonzalez, R. Alcantara, F. Nacimiento, G.F. Ortiz, J.L. Tirado, CrystEngComm, 16 (2014) 4602-4609.

[44] Y. Xu, M. Zhou, L. Wen, C. Wang, H. Zhao, Y. Mi, L. Liang, Q. Fu, M. Wu, Y. Lei Chem. Mater. 27 (2015) 4274-4280.

[45] S.-M. Oh, J.-Y. Hwang, C.S. Yoon, J. Lu, K. Amine, I. Belharouak, Y.-K. Sun, ACS Appl. Mater. Interfaces 6 (2014) 11295-11301.

[46] H. Xiong, H. Yildirim, E. V. Shevchenko, V. B. Prakapenka, B. Koo, M. D. Slater, M. Balasubramanian, S. K. R. S. Sankaranarayanan, J. P. Greeley, S.

Tepavcevic, N. M. Dimitrijevic, P. Podsiadlo, C. S. Johnson, T. Rajh J. Phys. Chem. C 116 (2012) 3181-3187.

[47] P. Balaya, A. J. Bhattacharyya, J. Jamnik, Y. F. Zhukovskii, E. A. Kotomin, J. Maier J. Power Sources 159 (2006) 171-178.

[48] Y. Wang, D.C. Alsmeyer, R.L. McCreery, Chem. Mater. 2 (1990) 557-563.

[49] A. Marmur Langmuir 19 (2003) 8343-8348.